In Situ Transmission Electron Microscopy Studies of the Solid–Liquid Interface

James M. Howe and Hiroyasu Saka

Abstract

In situ transmission electron microscopy (TEM) studies allow one to determine the structure, chemistry, and kinetic behavior of solid–liquid (S–L) interfaces with subnanometer spatial resolution. This article illustrates some important contributions of *in situ* TEM to our understanding of S–L interfaces in Al-Si alloys and liquid In particles in Al and Fe matrices. Four main areas are discussed: ordering in the liquid at a S–L interface, compositional changes across the interface, the kinetics and mechanisms of interface migration, and the contact angles and equilibrium melting temperature of small particles. Results from these studies reveal that (1) partially ordered layers form in the liquid at a Si{111} S–L interface in an Al-Si alloy, (2) the crystalline and compositional changes occur simultaneously across an Al S–L interface, (3) the Al interface is diffuse and its growth can be followed at velocities of a few nm/s at extremely low undercoolings, and (4) the melting temperature of In particles less than ~10 nm in diameter can be raised or lowered in Al or Fe, depending on the contact angle that the S–L interface makes at the three-phase junction. These results illustrate the benefits of *in situ* TEM for providing fundamental insight into the mechanisms that control the behavior of S–L interfaces in materials.

Keywords: *crystal growth, kinetics, phase transformation, powders, solid–liquid interfaces, transmission electron microscopy.*

Introduction

Experimental determination of the atomic structure and properties of solid–liquid (S–L) interfaces is inherently difficult because the interface is typically less than a few nanometers wide and is buried between two condensed phases, one of which is a liquid.[1,2] Transmission electron microscopy (TEM) allows one to see through inorganic materials with spatial and chemical resolutions on the atomic level,[3,4] so this technique is able to reveal the structural and chemical aspects of the interface experimentally.[5–10] In addition, samples examined in a TEM can be placed in holders capable of heating and cooling, so that the dynamics of interface motion can also be directly observed *in situ*.[11–14] One of the main limitations of *in situ* TEM is that the specimens are in a high vacuum, so it is only possible to use liquids with low vapor pressures or specimens that can contain the liquid phase within a thin solid layer.[15,16] The specimens must also be sufficiently thin, typically <500 nm, so that the electron beam can readily pass through them, and the S–L interface must be oriented parallel to the viewing direction, since one sees a projection of the structure on the detector in TEM.[3,4] These experimental considerations pose significant challenges. Nevertheless, *in situ* TEM has been able to reveal a wealth of information about the atomic structure and properties of S–L interfaces. This article describes some examples of important experimental results obtained on the S–L interface in Al-Si alloys and on the melting temperature of liquid In in Al and Fe matrices using this technique. These results cover a wide range of phenomena, including structural, chemical, kinetic, and thermodynamic aspects of the S–L interface.

Al Alloys as Model Experimental Systems

Al-Si and other Al alloys that contain low-melting-point insoluble particles are convenient for *in situ* TEM studies of the S–L interface for several reasons. The Al-Si system has a eutectic phase diagram with a eutectic composition of 12.2 at.% Si and a eutectic temperature of 577°C.[17] Thus, it is possible to heat alloys with compositions on either side of the eutectic composition slightly above the eutectic temperature to produce a system with a stable S–L interface. This may be accomplished by using small alloy particles or heating mixtures of Al and Si in various forms.[8,9,16,18–20] Such temperatures can be readily achieved using commercially available heating holders for TEM instruments, with or without water cooling. Although the vapor pressure of liquid Al-Si is high, the Al oxide layer that naturally forms on Al alloys is sufficient to contain the liquid in the sample in the high vacuum of the TEM, so evaporation is not a problem. Since the bonding in Al (metallic) and Si (covalent) is substantially different, this offers the possibility of observing different types of interface behavior, depending on the solid phase present. When low-melting-temperature alloys containing insoluble particles are used to form a S–L interface, such as Al-In and Fe-In, thin foils of the alloys containing small In particles are heated in the TEM until the particles melt. Since In is insoluble in both Al and Fe, it forms stable liquid droplets inside these matrices.[21] Other alloys such as Al-Pb and Al-Ar display similar behavior and have been studied by *in situ* TEM.[7,14]

Various modes of operation of the TEM can be used to determine the structure and properties of the S–L interface during *in situ* heating. These include electron diffraction, high-resolution TEM (HRTEM) and diffraction contrast imaging for determining the structure, and electron energy-loss spectroscopy (EELS) and energy-filtered TEM (EFTEM) imaging for determining the composition and bonding.[3,4,22] It is often not possible to obtain chemical information by energy-dispersive x-ray spectroscopy (EDXS) using typical commercial heating

holders, because they generate an infrared signal that floods the x-ray detector at temperatures above about 250°C. However, it is possible to obtain EDX spectra using special holders that employ resistively heated wires to both hold and heat the samples.[18] In order to perform quantitative crystal growth experiments, the heating and cooling characteristics of the sample holder must be carefully calibrated using standards with known transition temperatures, so that accurate undercoolings can be obtained.[19] Examples of research performed on several different types of Al-Si specimens, using different modes of TEM observation/characterization, on both Al-rich and Si-rich alloys are described in the following three sections. These are followed by a section discussing studies of insoluble In particles in Al and Fe matrices.[8,10,19,23,24]

Atomic Structure and Ordering

Figure 1a shows a HRTEM image of a S–L interface in an Al-Si alloy, obtained by resistively heating Al and Si particles together on a W filament.[8] In this case, the solid phase is Si and the liquid is an Al-Si alloy. The S–L interface is atomically flat and faceted along a Si{111} plane. The left side of Figure 1c shows a portion of the S–L interface at higher magnification. A transition region can be observed between the crystalline solid and liquid phases, where the contrast from the dumbbells of Si atoms (seen as dark ovals in the HRTEM image) is only about half as dark as in the perfect solid. An intensity profile taken across the S–L interface is also shown in the lower left in Figure 1c. The intensity profile has been inverted with respect to the image such that peaks in the profile represent the positions of atoms in the image, similar to the actual atomic density in the specimen. The intensity profile reveals the presence of three partially ordered layers in the liquid, parallel to the {111} plane of Si. Density profiles for two different models of the

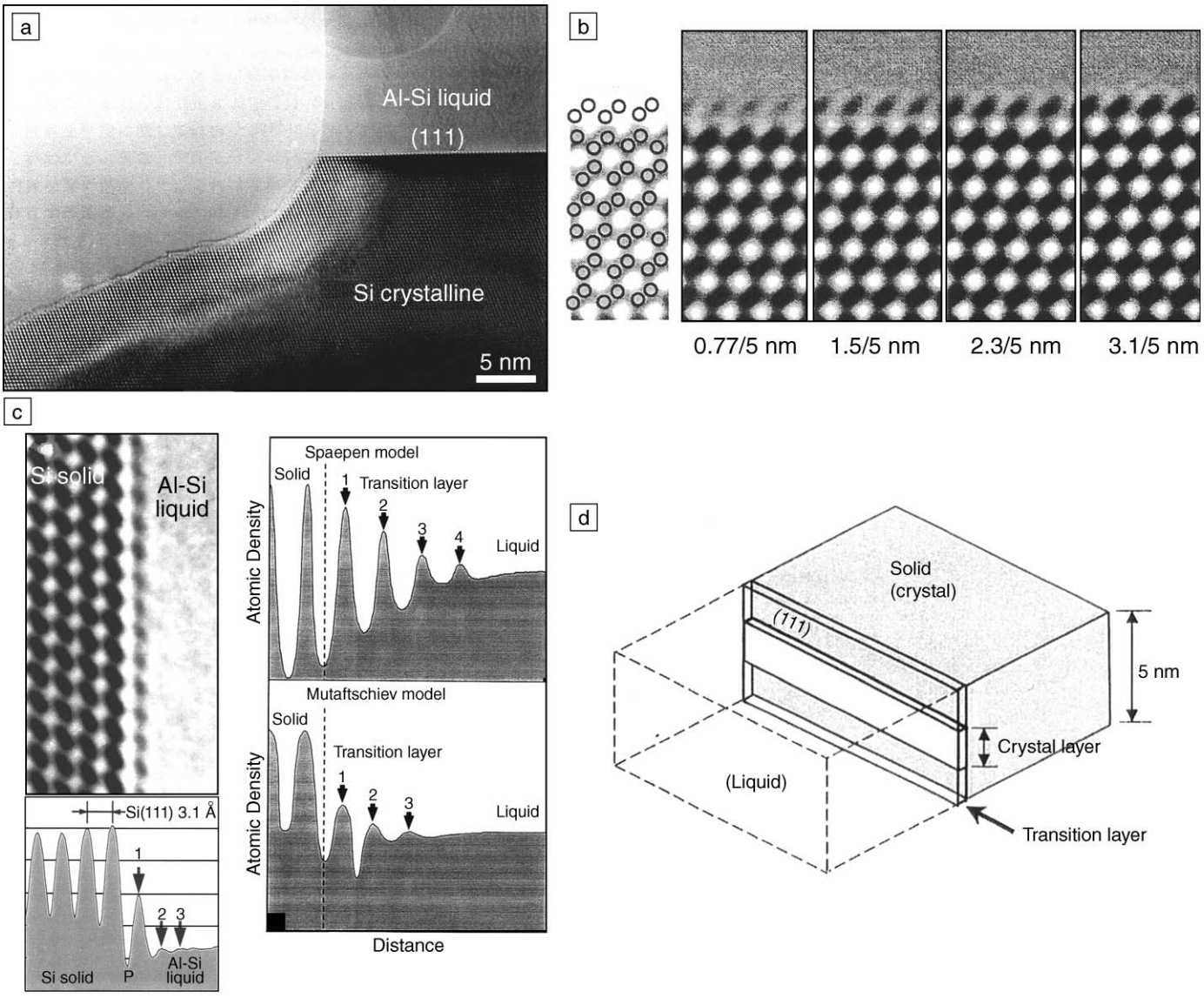

Figure 1. (a) High-resolution transmission electron microscope (HRTEM) image of a Si{111} solid–liquid (S–L) interface in an Al-Si alloy.[8] (b) Simulated HRTEM images of the interface, including a partially crystalline layer at the interface. (c) Enlargement of the S–L interface with a corresponding (inverted) intensity profile taken across the interface, and two models for the atomic density across a S–L interface. (d) Schematic illustration showing the crystalline layer used in the HRTEM image simulations.

atomic structure of a S–L interface, with different atomic densities at the interface, are shown schematically on the right side in Figure 1c. These models are based on dense random packing of hard spheres on a close-packed crystal surface. The behavior of the S–L interface with Si{111} as the solid phase more closely resembles the profile shown in the lower right in Figure 1c, although some features of both models are present in the experimental profile.

Figure 1b shows the results from HRTEM image simulations of the S–L interface, obtained by assuming that the first transition layer in the image is a mixture of Al-Si liquid and partially solid Si{111}. This layer was modeled by adding an additional atomic layer on top of the Si{111} surface partway through the thickness of the sample, as illustrated schematically in Figure 1d. The proportion of solid to liquid phase was varied in the simulations for a constant sample thickness of 5 nm, as indicated below each simulated image in Figure 1b, with the top number indicating the thickness of the crystalline region. The closest match in appearance with the experimental image was obtained when the thickness of the crystalline region in the first layer at the S–L interface was between 1.5–2.3 nm. This result indicates that not only is there ordering in the first several liquid layers parallel to the interface, but there is also strong two-dimensional ordering within the first layer of liquid, since the positions of the dark ovals in this layer are highly regular in the HRTEM image and accompanying simulations.

Figure 2 shows the dynamic behavior of another Si{111} S–L interface during crystal growth. The S–L interface is moving from right to left in the series of images, labeled (a)–(f) on the left side in Figure 2. Figure 2g shows intensity profiles taken across the S–L interfaces in (a)–(f). In Figure 2a, the interface is at position 1 in Figure 2g. In Figure 2b, 1/30 s later, it has advanced to position 2 in Figure 2g. The contrast of the atomic columns in the region between positions 1 and 2 is significantly lower than that of the solid matrix, but higher than that of the liquid. This suggests that the region between positions 1 and 2 is a mixture of solid and liquid phases. In other words, atoms in this region are in a partially molten state. In Figure 2c, the S–L interface has advanced to position 3. Again, the lattice fringes between positions 1 and 3 are fainter than those of the crystalline solid. After 5/30 s, the contrast in this region becomes comparable to that of the solid, again with the S–L interface atomically faceted along the Si{111} plane. The average velocity of the S–L interface in this series of images was estimated as 20 nm/s.[8] These results suggest that cooperative organization of many close-packed layers of Si atoms occurs under the influence of a driving force for crystal growth at the Si{111} interface.

Interface Composition

Energy-filtered TEM (EFTEM) imaging was used to map the composition of a S–L interface in a partially molten Al-11.6at.%Si alloy particle *in situ*, and the composition was compared with the degree of crystallinity at the interface, as defined by the diffraction contrast present in a bright-field (BF) TEM image.[10] Figures 3a and 3b show the resulting diffraction contrast image and Al composition map, respectively, in the particle. In Figure 3a, the crystalline region is strongly diffracting, which causes it to appear dark, while in Figure 3b, the brightness in the image is proportional to the Al concentration. Also shown in Figures 3a and 3b are two regions where intensity profiles were taken across the S–L interface, away from the edge of the particle. Only the profile labeled Region 2 is discussed here, since it is the narrowest profile.

The normalized intensity profile from Region 2 is plotted in Figure 3c. This figure shows that the diffraction and Al composition intensity profiles are complementary, that is, inversely related, and that the interface can be defined both structurally and compositionally with subnanometer resolution. In the profiles, the diffraction contrast in the liquid decreases at a nearly constant rate up to the interface, where it drops sharply, before decreasing further in the crystalline solid at a constant rate similar to that in the liquid. The Al composition profile is fairly constant in both the solid and liquid and changes rapidly at the interface. The width of the interface, determined by considering both the diffracted and compositional intensities, was 2.9 nm, as indicated by the vertical lines in Figure 3c. This is equivalent to a distance of about seven unit cells of Al (lattice parameter = 0.405 nm). The fact that the changes in diffraction and compositional contrast across the interface occur over similar distances indicates that the interface adopts a configuration in which the structure and composition are related and change simultaneously from the crystalline solid to liquid states.

The interface width of 2.9 nm shown in Figure 3c represents the maximum width of the interface, including any smearing that may occur due to curvature of the interface or overlapping of the solid and liquid through the thickness of the particle along the electron beam direction. Additional studies[19] performed at the aluminum oxide–vacuum interface to assess the effect of curvature on resolution and smearing in BF and EFTEM imaging have shown that curvature typically does not blur the images more than 1 nm. If it is assumed that this effect is present in Figure 3c, then the actual interface width is more likely about 1.9 nm (or approximately 5 unit cells of Al), which is the same as the minimum interface width that has been experimentally observed by diffraction contrast in these particles so far.[19] Note that this is consid-

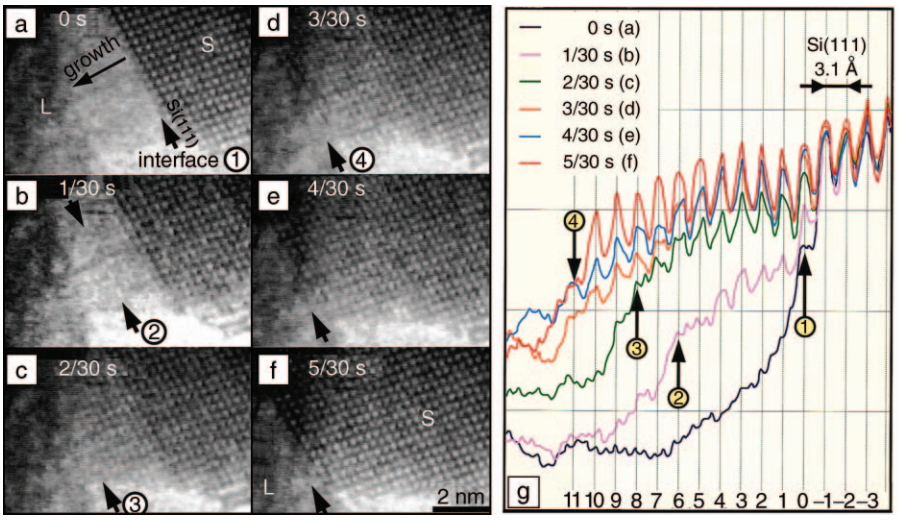

Figure 2. (a)–(f) Series of video frames (1/30 s apart), showing motion of a Si{111} solid–liquid interface.[8] (g) Corresponding intensity profiles taken across the moving interface, showing the development of crystallinity with time. See text for discussion. The numbers at the bottom in (g) indicate the number of Si {111} planes to the left (+) and right (–) of the initial position (0) in (a).

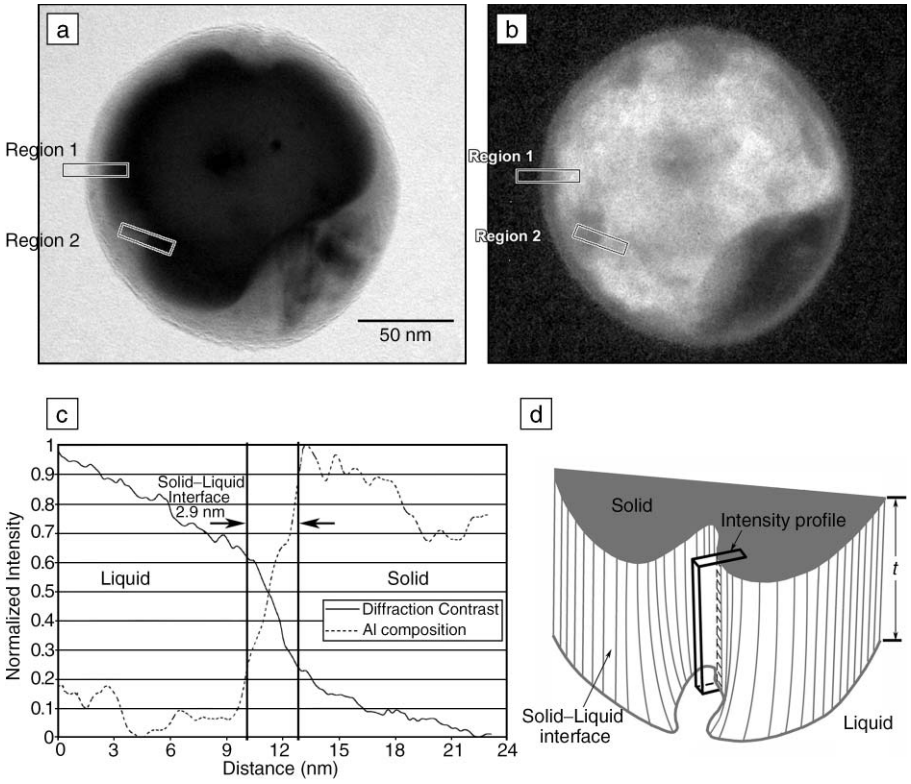

*Figure 3. (a) Bright-field transmission electron microscope (TEM) image of the solid–liquid (S–L) interface in a partially molten Al-Si particle.[10] (b) Corresponding Al composition map (a non-diffracting jump-ratio image calculated from energy-filtered TEM images taken at 95 eV and 125 eV energy loss.) (c) Intensity profiles from area marked Region 2 in (a) and (b), with the width of the S–L interface indicated. (d) A schematic of the S–L interface in Region 2 where the intensity profiles were taken (*t *is thickness).*

erably wider than at the Si{111} S–L interface in Figure 1.

A schematic of the S–L interface in the region of the intensity profile in Figures 3a and 3b is shown in Figure 3d. Only the solid portion of the interface is sketched in the figure. The schematic shows how the interface could appear approximately 2 nm wide in projection in the intensity profile, either by being atomically sharp but bending slightly through the sample thickness (t), or by being straight but diffuse over a similar width. A combination of these two possibilities with smaller magnitudes could also yield structural and compositional intensity changes no more than 2 nm wide across the S–L interface in BF and EFTEM images. It is difficult to distinguish between these two effects based only on the contrast in such images, but in any case, the results in Figure 3c indicate that the structural and compositional changes are closely correlated, to within fractions of a nanometer at the S–L interface. Additional information provided in the next section indicates that this S–L interface is most likely diffuse.[2,25,26]

Interface Kinetics and Undercooling

The high spatial resolution obtained in TEM allows one to determine the kinetics of interface motion at a level unprecedented by other techniques.[2–4] This is particularly important when trying to determine the mechanisms of interface motion, as illustrated by the following example. Similar kinds of experiments can be performed on practically any kind of transformation interface.[11,12]

The kinetic behavior of the S–L interface in a partially molten Al-11.6at.%Si alloy particle was investigated by inducing crystal growth at various undercoolings (through various heating-holder cooling rates) and measuring the corresponding interfacial velocities.[19] Figure 4a shows the TEM image and corresponding diffraction pattern of a 400 nm particle, which was oriented on a ⟨110⟩ zone axis. This particle was heated to a partially molten state, as seen in the video frame in Figure 4b. Next, it was completely solidified by cooling, as in Figure 4c. During cooling, the average velocity of the S–L interface was determined from the total distance it traveled, divided by the time over which crystal growth occurred. The region of the interface where the velocity was measured was the lower-right portion of the particle in Figure 4b. This region of the interface appears flat and was inclined 13° from the ⟨111⟩ direction. The contrast is low in Figures 4b and 4c because they are single-frame video images.

The results of the crystal growth experiments are plotted in Figure 4d. This graph shows the S–L interface velocity plotted against the corresponding furnace current decrease, which is linearly related to the undercooling. In Figure 4d, the crystal growth velocity versus driving force relationships for three possible interface growth mechanisms were fitted to the data. In the case of an atomically smooth, defect-free interface, growth occurs by two-dimensional nucleation and growth (2DNG), which produces an interfacial growth rate that depends on the undercooling in an Arrhenius type relationship.[2,25–27] If the crystalline portion of the interface contains screw dislocations, these defects act as regions where liquid atoms easily attach to the solid, and the screw dislocation growth (SDG) rate is proportional to the square of the undercooling. For a rough interface, growth occurs rapidly by continuous atomic attachment everywhere along the interface at very low undercoolings (e.g., ~0.0001°C). This mechanism has a growth rate that is linear with undercooling.[25–27] The data in Figure 4d closely follow the linear behavior associated with a continuous growth mechanism, as seen by the correlation factor (R^2) value of 0.88.

Crystal growth depends on two processes: the mechanism of atomic attachment at the interface and diffusion of excess solute in the liquid away from the more pure (in this case) solid. The controlling process is that which occurs at a slower rate. The following analysis of the Al-Si S–L interface illustrates how it is possible to distinguish between the two processes using appropriate kinetic and thermodynamic data.

Since the observed behavior of the interfacial velocity versus undercooling was linear in Figure 4d, the interface could only grow by an interface-controlled mechanism if that mechanism was by continuous growth. To determine the exact growth regime, the linear growth constants for continuous, K_I, and diffusion-controlled, K_D, growth were compared using the following general equations:[28,29]

$$K_I = \beta D_L L / aRT_m^2 , \quad (1)$$

where D_L is the diffusivity of the liquid, L is the heat of melting, a is the liquid jump distance (or approximately the close-packed

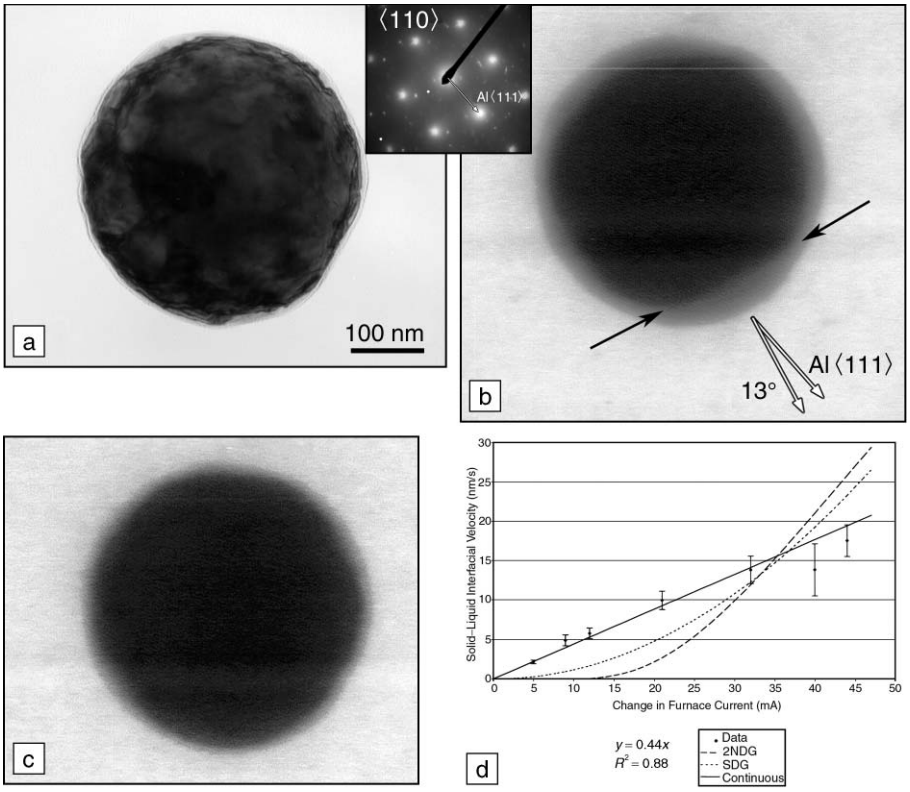

Figure 4. (a) Transmission electron microscopy image of a crystalline Al-Si particle, with corresponding ⟨110⟩electron diffraction pattern (inset) showing the particle crystallography.[19] (b) The particle in a partially molten state with a flat portion of the solid–liquid (S–L) interface indicated by arrows. (c) The same particle after lowering the temperature to grow the S–L interface. (d) Growth kinetics of the S–L interface in (b), produced by decreasing the current to the heating holder. The change in temperature is linearly related to the change in furnace current. See text for details.

interplanar spacing in the solid), R is the universal gas constant, T_m is the melting temperature, and β is a correction factor, which varies between 1 and 100.[28] For diffusion-controlled growth,

$$K_D = D_L/rm_L(C - C_0)\,, \qquad (2)$$

where r is the radius of the spherical particle, m_L is the slope of the liquidus line in the phase diagram, C is the composition of the solid formed, and C_0 is the composition of the liquid at the interface.[29]

The appropriate parameters for the growth constants of an Al-Si particle with a 200 nm radius are shown in Table I. For typical metals, the value of K_I is around 1.0 m/s K, and the calculated values in Table I show reasonable agreement, with values ranging from $5.4 < K_I < 0.054$ m/s K. In addition, Table I shows that $K_D < K_I$, which indicates that crystal growth is most likely controlled by diffusion of Si away from the interface rather than by the mechanism of atomic attachment; in other words, K_D is the rate-limiting quantity. Figure 4d shows that the growth velocity depended linearly on the furnace current, with a slope of 0.44 nm/s mA. Thus, a change in the furnace current produced a linear change in undercooling, with a proportionality constant of $0.44/(10^9 K_D) = 1.2 \times 10^{-8}$ K/mA. The smallest interfacial velocity observed in Figure 4d was 2.2 nm/s for a change in furnace current of 5 mA. Thus, this growth velocity was driven by an undercooling of 5.8×10^{-8} K, as determined by the diffusion-controlled growth equation:[29]

$$V_D = K_D \Delta T\,, \qquad (3)$$

where V_D is the interface velocity and ΔT is the undercooling. It is evident that *in situ* TEM allows one to measure the velocities and undercoolings at S–L interfaces with high resolution and accuracy.

Size Dependence of Melting Temperature

It is well known that the melting temperature of a metallic particle with a free surface decreases with decreasing particle size, particularly below 10 nm in diameter.[2,30] However, this is not necessarily the case when the particles are embedded in a matrix. A typical example of this occurs for In particles embedded in an Al matrix.[23] The melting temperature of pure In is 155°C, and there is virtually no mutual solubility between In and Al below 200°C. Figure 5a shows a bright-field TEM image of In particles embedded in an Al matrix at ~155°C with a corresponding inset ⟨110⟩ diffraction pattern. Particles that display moiré fringes (such as those labeled C, D, and E) are crystalline In, while those without moiré fringes (such as particles A and B) are liquid In. Comparing the particle sizes of these two groups, it is clear that the smaller particles are crystalline, while the larger particles have melted. Particles F and G are of particular interest in that liquid In has nucleated at the {100} facets (indicated by

Table I. Comparison of Kinetic Growth Constants for Interface-Controlled Continuous Growth versus Diffusion-Controlled Growth in an Al-Si Particle with a 200 nm Radius.

Continuous Growth Parameters	Symbol	Value
Diffusivity of the liquid	D_L	5.5×10^{-9} m²/s K
Correction factor	β	~1–100
Enthalpy of melting	L	13740 J/mol
Liquid jump distance	a	2.34×10^{-10} m
Universal gas constant	R	8.314 J/mol K
Melting temperature	T_m	850 K
Growth constant (continuous)	K_I	~5.4×10^{-2} m/s K
Diffusion-Controlled Growth Parameters		
Diffusivity of the liquid	D_L	5.5×10^{-9} m²/s K
Radius of the particle	r	2×10^{-7} m
Slope of the liquidus line	m_L	6.8 K
Composition of the solid formed	C	0.985 at.% Al
Composition of the liquid at the interface	C_0	0.878 at.% Al
Growth constant (diffusion-controlled)	K_D	3.8×10^{-2} m/s K

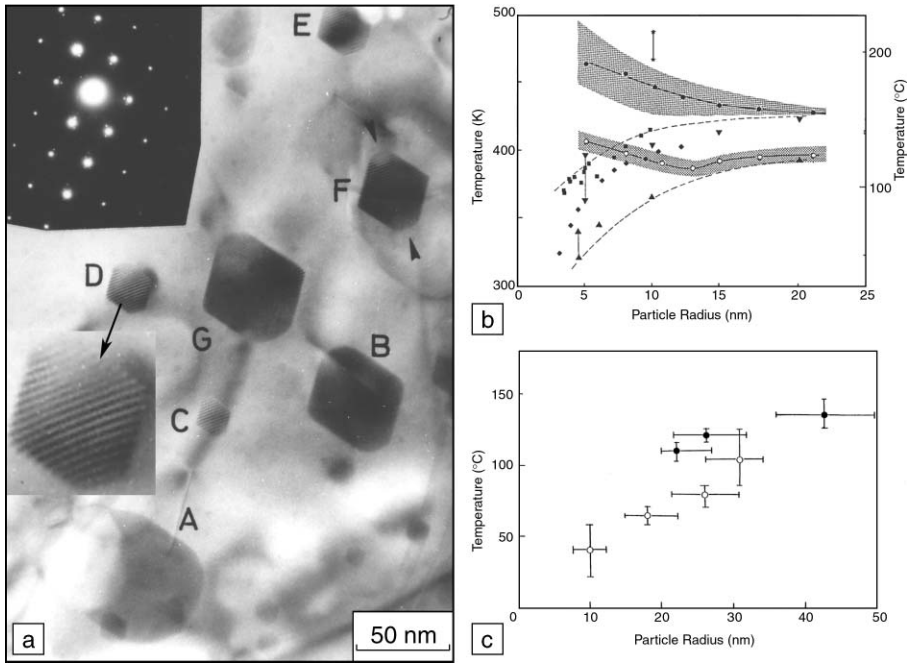

Figure 5. (a) TEM image of In particles in Al at ~155°C with a corresponding inset ⟨110⟩ diffraction pattern.[23] Particle D is shown enlarged to better reveal the moiré fringes. (b) Corresponding melting temperature of the In particles versus particle size (the triangular and square data points apply to other systems that are not discussed here). (c) Melting temperature of In particles in Fe as a function of particle size.

arrows for particle F). Figure 5b shows a plot of the melting temperature of the In particles as a function of particle size (shaded data). The melting temperature clearly increases below 10 nm. Figure 5c shows another example of the melting behavior of In particles, but this time embedded in a Fe matrix.[24] In this case, the melting temperature decreases with decreasing particle size. This difference in melting behavior of In particles embedded in Al and Fe matrices can be explained as follows.

Thermodynamic models[31–33] suggest that the melting point T of small particles varies inversely with the particle radius r and is proportional to the difference in surface energy between the solid and liquid states, that is,

$$T_0 - T/T_0 = k(\gamma_{sv}/\rho_s - \gamma_{lv}/\rho_l)/rL\,, \quad (4)$$

where T_0 is the bulk melting temperature, k is a positive constant, L is the latent heat of melting per unit mass, ρ_s and ρ_l are the densities of the solid and liquid phases, respectively, and γ_{sv} and γ_{lv} are the surface energies of the solid and liquid, respectively. Using the approximation that $\rho_s = \rho_l = \rho$, Equation 4 can be rewritten as

$$T_0 - T/T_0 = k(\gamma_{sv} - \gamma_{lv})/rL\rho\,. \quad (5)$$

For particles with a free surface, $\gamma_{sv} - \gamma_{lv} > 0$ and $T_0 > T$, so that depression of the melting temperature is observed. For particles embedded in a matrix, γ_{sv} and γ_{lv} should be replaced with γ_{sm} and γ_{lm}, respectively, where γ_{sm} and γ_{lm} are the interfacial energies between the solid and matrix, and liquid and matrix, respectively. The quantities γ_{sm} and γ_{lm} are related to γ_{sl} and the contact angle θ through Young's equation:

$$\gamma_{sm}\gamma_{lm} = \gamma_{sl}\cos\gamma\,, \quad (6)$$

where γ_{sl} is the S–L interfacial energy. Substituting Equation 6 into Equation 5 yields

$$T_0 - T/T_0 = k(\gamma_{sl}\cos\gamma)/rL\gamma\,. \quad (7)$$

Figures 6a and 6b show electron diffraction patterns from Al-In and Fe-In samples, respectively. For Al-In (Figure 6a), there is a cube-on-cube orientation relationship between the particles and matrix, while in the case of Fe-In (Figure 6b), there is no such simple or rational orientation relationship.[23,24] The presence of a cube-on-cube orientation relationship for solid In particles in Al suggests that the interfacial energy between the solid In particles and the Al matrix is likely low, while this is not the case for Fe-In. This feature is supported by observing the contact angles, θ, of the S–L interface in partially molten In particles in the Al and Fe matrices. Figures 6c and 6d show TEM images of partially molten In particles embedded in Al and Fe matrices, respectively. For Al-In (Figure 6c), $\theta > 90°$, while for Fe-In (Figure 6d), $\theta < 90°$, indicating that elevation and depression of the melting temperature should occur for the Al-In and Fe-In cases, respectively. These results illustrate how *in situ* TEM can be used to determine the contact angles associated with the S–L interface in small, embedded particles in order to understand their melting behavior. Such experiments can be performed to understand similar phenomena in many other systems.

Summary

The results presented in this article show how *in situ* TEM can be used to obtain information about the structural, chemical, kinetic, and thermodynamic properties of solid–liquid interfaces. The main advantages of *in situ* TEM for obtaining such information as compared with other techniques are its atomic-level chemical and spatial resolution, the ability to see through inorganic materials and the ability to directly observe dynamic processes that occur at the interface in response to heating or cooling. Only a limited number of alloy systems have been investigated in detail, such as the Al alloys described in this article. There are many opportunities for new systems and experiments to be performed to further understand the behavior of S–L interfaces in materials. Specific conclusions obtained from the S–L interface studies described in this article are as follows:

1. Intensity profiles taken across HRTEM images of Si{111} S–L interfaces reveal the presence of partially ordered layers in the liquid, parallel to the interface, and there is evidence for two-dimensional ordering within the first layer of liquid. HRTEM images of interface motion suggest that cooperative organization of many {111} planes of Si atoms occurs under the influence of a driving force for crystal growth.
2. The change in crystallinity at an Al S–L interface, as defined by diffraction contrast, is accompanied by a corresponding change in composition across the interface, as determined from intensity profiles in Al composition maps. Thus, the structural and compositional changes are strongly correlated at the S–L interface and appear to occur simultaneously over a distance of no more than about 2 nm, which likely represents the diffuseness of the S–L interface.
3. Using a calibrated heating holder, it is possible to study the motion of S–L interfaces with subnanometer spatial resolution and growth velocities as low as ~2 nm/s.

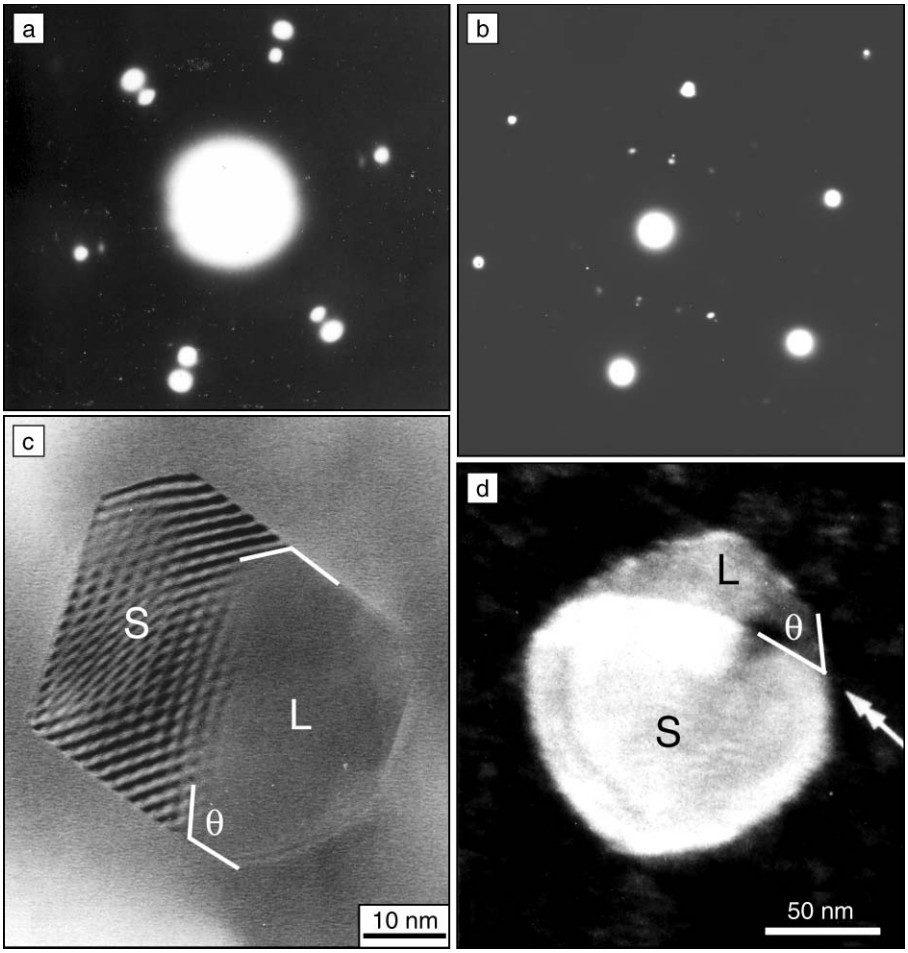

Figure 6. Electron diffraction patterns taken from In particles in (a) Al and (b) Fe matrices.[23,24] Note the alignment of diffraction spots between the In particles and matrix in (a), but not in (b). Transmission electron microscopy images of partially molten In particles in (c) Al and (d) Fe, with contact angles indicated.

Growth of Al-rich solid into liquid Al-Si alloy occurs in the diffusion-controlled regime by a continuous mechanism of atomic attachment, at undercoolings as low as 5.8×10^{-8} K.

4. The equilibrium melting temperature of small particles embedded in a matrix can be elevated or depressed, depending on the contact angle that the S–L interface makes at the junction among the solid, liquid, and matrix phases.

Acknowledgments

J.M. Howe gratefully acknowledges support for this research from the U.S. National Science Foundation under grant DMR-9908855, as well as the collaboration of Dr. K.T. Moore and Mr. G.A. Storaske on the Al-Si work. H. Saka acknowledges support from the Japan Society for the Promotion of Science under grants-in-aid for scientific research (contract 14205092).

References

1. E. Johnson, *Science* **296** (2002) p. 477.
2. J.M. Howe, *Interfaces in Materials* (John Wiley & Sons, New York, 1997) pp. 219–291.
3. D.B. Williams and C.B. Carter, *Transmission Electron Microscopy: A Textbook for Materials Science* (Plenum Press, New York, 1996).
4. B. Fultz and J.M. Howe, *Transmission Electron Microscopy and Diffractometry of Materials* (Springer-Verlag, Berlin, 2001).
5. K. Sasaki and H. Saka, *Philos. Mag. A.* **63** (1991) p. 1207.
6. J.M. Howe, *Philos. Mag. A* **74** (1996) p. 761.
7. S.E. Donneley, R.C. Birtcher, C.W. Allen, I. Morrison, K. Furuya, M. Song, K. Mitsuishi, and U. Dahmen, *Science* **296** (2002) p. 507.
8. S. Arai, S. Tsukimoto, H. Miyai, and H. Saka, *J. Electron Microsc.* **48** (1999) p. 317.
9. S. Tsukimoto, S. Arai, M. Konno, T. Kamino, K. Sasaki, and H. Saka, *J. Microsc.* **203** (2000) p. 17.
10. G.A. Storaska, K.T. Moore, and J.M. Howe, *Philos. Mag. A* **84** (2004) 2619.
11. R. Sinclair, *Acta Cryst.* **A44** (1988) p. 26.
12. J.M. Howe, *Mater. Trans. JIM* **39** (1998) p. 965.
13. H. Saka, K. Sasaki, T. Ohashi, I. Ohtsuka, T. Kamino, and M. Tomita, *Ultramicrosc.* **39** (1991) p. 110.
14. H. Gabrisch, L. Kjeldgaard, E. Johnson, and U. Dahmen, *Acta Metall.* **49** (2001) p. 4259.
15. S. Arai, S. Tsukimoto, and H. Saka, *Microsc. Microanal.* **4** (1998) p. 264.
16. G.A. Storaska and J.M. Howe, *Mater. Sci. Eng., A* **368** (2004) p. 183.
17. J.L. Murray and A.J. McAlister, *Bull. Alloy Phase Diagrams* **5** (1984) p. 74.
18. T. Kamino, K. Sasaki, and H. Saka, *Microsc. Microanal.* **3** (1997) p. 393.
19. G.A. Storaska, MS thesis, University of Virginia (2001).
20. T. Yokota, J.M. Howe, and M. Murayama, *Phys. Rev. Lett.* **91** 265504 (2003).
21. J.L. Murray, *Bull. Alloy Phase Diagrams* **4** (1983) p. 30.
22. R.F. Egerton, *Electron Energy-Loss Spectroscopy in the Electron Microscope,* 2nd Ed. (Plenum Press, New York, 1996).
23. K. Sasaki and H. Saka, *Philos. Mag., A* **63** (1991) p. 1207.
24. T. Ohashi, K. Kuroda, and H. Saka, *Philos. Mag., B* **65** (1992) p. 1041.
25. J.W. Cahn, *Acta Metall.* **8** (1960) p. 554.
26. J.W. Cahn, W.B. Hillig, and G.W. Sears, *Acta Metall.* **12** (1964) p. 1421.
27. M.C. Flemings, *Solidification Processing* (McGraw-Hill, New York, 1974) pp. 31, 284, 301, 307, and 322.
28. S.D. Peteves and R. Abbaschian, *Metall. Trans., A* **22** (1991) pp. 1259 and 1271.
29. J.W. Cahn, in *Crystal Growth* (Pergamon Press, New York, 1957) p. 681.
30. J. Borel, *Surf. Sci.* **106** (1981) p. 1.
31. R. Kofman, P. Cheyssac, A. Aouj, Y. Lereah, G. Deudtscher, T. Ben-David, J.M. Penisson, and A. Bourret, *Surf. Sci.* **303** (1994) p. 231.
32. P. Pawlow, *Z. Phys. Chem.* **65** (1909) p. 545.
33. G.L. Allen, R.A. Bayles, W.W. Gile, and W.A. Jesser, *Thin Solid Films* **144** (1986) p. 297.

□